PEMFC ELECTROCHEMISTRY: SIMULATION OF NONEQUILIBRIUM SURFACE CHEMISTRY ON 3-DIMENSIONAL GEOMETRIES

Varun Rai, Masoud Aryanpour, Abhishek Dhanda, Stephen Walch, and Heinz Pitsch
Mechanical Engineering Department, Stanford University, CA 94305, USA

Abstract

The performance of polymer exchange membrane fuel cells is known to be strongly influenced by the electrochemical reactions occurring in the cathode catalyst layer. The dynamics of the elementary reaction steps in the oxygen reduction reaction on platinum based catalysts are investigated to provide a better understanding of the cathode overpotential. We present a new approach using Dynamic Monte Carlo (DMC) simulations for providing an accurate description of the kinetics of ORR on real 3D nanoparticle geometries. Simulations of the ORR on model cubo-octahedral shaped nanoparticle are presented and are found to predict experimentally observed coverages of O-containing species with good accuracy.

INTRODUCTION

Low operating temperatures, quiet operation, and high theoretical efficiencies, among a host of other features, make Polymer Electrolyte Membrane fuel cells (PEMFC) viable for near-term commercialization, especially for portable electronics devices and applications in transportation [1]. Carbon-supported platinum catalysts are commonly used in the catalyst layer of PEMFC due to their high activity for oxygen reduction reactions (ORR). However, the sluggish electrochemical reactions (ECR) catalyzed by nanometer size metal particles at the electrodes limit the performance of these cells. The ECR have potential-dependent activation energies [2], which can lead to high coverage of the electrocatalyst surface at the cathode by oxygen-containing species (O/OH) [3], potentially causing an increased overpotential. Hence, a detailed study of the chemical kinetics at the cathode is important for a better understanding of the dynamics of surface reactions in such catalytic systems.

The nanometer size particles catalyzing the ECR have spatially discontinuous variation of catalytic activity on their surfaces. Specifically, the edge/corner sites of these nanoparticles behave very differently from the sites located on the faces [4, 5]. Furthermore, the chemical species already adsorbed on the particle surface might interact with each other due to electronic effects [3, 6, 7]. Such local phenomena are important as they can change the steady state of the system significantly, and can lead to nonlinear and/or chaotic behavior in some catalytic systems [8, 9]. The mean field approach as an environment-averaged approximation cannot accommodate the details of such local phenomena and has been shown to provide poor description of the kinetics in such situations [10, 11]. To overcome these limitations we apply Dynamic Monte Carlo (DMC) simulations [12] for ORR on Pt nanoparticles, as this approach admits an accurate description of surface reaction kinetics.

Application of DMC has been limited mostly to simulating 2D, single crystal catalytic systems [11, 13]. In this work, we present a novel approach, 3-DMC, for performing DMC simulations on realistic 3D nanoparticle geometries used in electrocatalysis. Our method allows the simultaneous presence of different crystal planes, edges, and corner sites within the same simulation and can account for lateral interactions of adsorbed species and different types of surface sites such as atop, bridge, and hollow sites. The Variable Step Size Method (VSSM) algorithm [12], also referred to as the Continuous Time Monte Carlo (CTMC) [14], has been implemented in 3-DMC. This algorithm will be briefly described in the next section followed by some details of the 3-DMC implementation. The set of chemical and electrochemical reactions used to describe oxygen reduction on Pt-nanoparticles in PEMFC will be discussed next, followed by the results of DMC simulations of the chemistry on cubo-octahedral shaped Pt-nanoparticles.

DMC SIMULATIONS

Algorithm

The DMC method was originally introduced by Bortz et al. [15] for studying spin reduction of an Ising model, and has since been adapted for surface chemistry simulations for a number of applications [8, 9, 11, 13, 16, 17, 18]. In DMC, the catalyst surface is modeled by a series of *sites* where each site corresponds to a potential location of an adspecies on the real catalyst surface. The complete specification of adspecies present at every site describes a *configuration* or *state* of the system and is stored in a vector $\mathbf{n}$. The probability that the lattice at time t appears in a certain configuration $\mathbf{n}$ is denoted by $p_{\mathbf{n}}(t)$. A *microprocess* is used to denote an elementary reaction step in the mechanism. If a microprocess can take place at some location on the catalyst surface in the current configuration then it is referred to as an *enabled event* or just event. An event changes a configuration into a different configuration and is characterized by both of these configurations. Note that not all microprocesses are possible for each possible configuration. The probability per unit time that a particular reaction transforms configuration $\mathbf{n}'$ into configuration $\mathbf{n}$ is called the transition probability $w_{\mathbf{n}\mathbf{n}'}$, which can be interpreted as a microscopic analog of a reaction rate, and depends on the configuration. Each possible transition corresponds to a specific microprocess and is determined using the rate constant of the corresponding reaction step. The time evolution and the dynamics of this system are described by the so called Master equation. This is a differential equation for the probability $p_{\mathbf{n}}(t)$ of finding the system in a configuration $\mathbf{n}$, which is derived from first principles, and can be written as

$$\frac{dp_{\mathbf{n}}(t)}{dt} = \sum_{\mathbf{n}'\neq\mathbf{n}} \left[w_{\mathbf{n}\mathbf{n}'} p_{\mathbf{n}'}(t) - w_{\mathbf{n}'\mathbf{n}} p_{\mathbf{n}}(t) \right]. \tag{1}$$

$p_{\mathbf{n}}$ is a scalar function that has to be solved in N dimensions, where N is the number of possible configurations. It is obvious that a direct solution of this equation is not possible for more than a few sites. The master equation, therefore, is usually solved using the stochastic approach of Monte Carlo methods. Solution methods have been described by Binder and Heermann [19] and issues specific to electrocatalytic chemistry have been discussed by Brown et al. [20].

The most commonly used algorithms for DMC are the Random Selection Method (RSM) [21, 22], VSSM, and the First Reaction Method (FRM), which is also called the discrete event selection method. In RSM, the simplest of the three algorithms, the current state of the surface does not influence the selection of the next event. In each step of the method, a site and a microprocess are selected randomly. Then, if the selected microprocess is enabled at this particular site, the lattice is changed accordingly. It is a good choice for simple chemical mechanisms, but can be inefficient in even moderately complex situations because of the occurrence of so called null events [14]. These are trials that do not lead to any change in the configuration of the surface, which can make the evolution of the system towards the steady state slow for mechanisms where one or more of the fast reaction steps are not frequently enabled on the surface. Another disadvantage of RSM is that relating the evolution of the system to real time is only approximate and not straightforward, especially for complex mechanisms. The FRM algorithm relies on explicitly storing every single enabled event on the surface along with the corresponding time of occurrence. The next event selected is then the one which is the nearest in time. This method is the most general of the three algorithms for DMC. In fact, it also allows for simulating systems with time varying rate constants [23, 13]. The computation time per simulated reaction in FRM depends on the lattice size, a fact that is potentially limiting for simulating systems of large lattice size. VSSM turns out to be the best choice for most cases which do not involve time varying rate constants [12]. This algorithm was hence chosen for the present work. A simple description of VSSM is presented next.

Let $\mathbf{n}$ denote the current configuration, and $\Omega_{\mathbf{n}}^{(i)}$ and $k^{(i)}$ denote the number of enabled events and the rate coefficient for a microprocess i, respectively. Then

$$\Gamma_{\mathbf{n}}^{(i)} = \Omega_{\mathbf{n}}^{(i)} k^{(i)}, \text{ and } \Gamma_{\mathbf{n}} = \sum_i \Gamma_{\mathbf{n}}^{(i)}, \tag{2}$$

where $\Gamma_{\mathbf{n}}$ denotes the total transition probability per unit time. The j^{th} microprocess is then selected based on a uniform random number r in [0,1] such that

$$\frac{\sum_{i=1}^{j-1} \Gamma_{\mathbf{n}}^{(i)}}{\Gamma_T} \leqslant r < \frac{\sum_{i=1}^{j} \Gamma_{\mathbf{n}}^{(i)}}{\Gamma_T}. \tag{3}$$

Depending on the selected microprocess, a site or a pair of sites where the microprocess will be performed can be selected in two different ways. In the first method, the selection is made randomly over the entire surface until a matching location is found where the microprocess can be carried out [10]. In the second method, the site is selected from a list L_j that stores all the site locations where microprocess j is enabled. Of course, in the latter approach, the lists L_j need to be updated at every step. Finally the system time is updated according to:

$$\Delta t = -\frac{\ln(\xi)}{\Omega_T \Gamma_T}, \tag{4}$$

where ξ is a uniform random number in (0,1). A more general formulation of VSSM used here is very similar to the algorithm just described, but it also uses the concept of *classes* wherein every event is classified based on the adspecies in its microenvironment [14]. Details about the mathematical foundation and comparative studies of the different algorithms can be found elsewhere [12, 14, 19].

3-DMC

This method has been implemented in the new 3-DMC simulation code which allows the application of DMC simulations for complex catalyst surfaces. A unified representation of the surface sites, wherein each site on the catalyst surface is linked to all its neighboring sites is required to do such simulations. Such a representation will henceforth be termed a *connected representation*. A connected representation for planar surfaces (for e.g., (111) or (100)) is fairly simple to obtain. But real catalyst nanoparticles used in PEMFC have edges and corners. For example, in cubo-octahedral shaped nanoparticles, the surface atoms are arranged on eight (111) and six (100) crystallographic surfaces connected by thirty-six edges and twenty-four corner atoms. Owing to their different catalytic behavior [4, 5], directly accounting for edge and corner atoms can be helpful in a more accurate description of surface kinetics. Obtaining connected representations for such real surfaces is nontrivial, mainly because of the difference in atomic arrangements on the facets adjoining the edge/corner sites. In the following, we demonstrate our approach for generating a connected representation using the example of a cubo-octahedral nanoparticle (Fig. 1a).

Defining the surface: The coordinates of the corner atoms are sufficient to fully specify a single facet, and hence to specify the shape and size of the complete surface. The coordinates of the corner atoms and the specification of corner atoms corresponding to each facet are inputs to the program in the form of numerical arrays.

Breaking the problem: The surface consists of simple hexagonal (111) and rectangular (100) facets. As pointed out before, a connected representation for planar surfaces is relatively simple. As a first step then, individual connected representations for all facets are obtained separately. The representation involves implicit numbering of the edges for every facet as demonstrated in Fig. 2. The faces are also numbered in a convenient manner.

Setting the coordinates: Coordinates of all other atoms present in the central portion of a facet are computed by pairing up the edge atoms. For example, in the diagram on the left in Fig. 2, C_0 and C_2 are used to get the coordinates of E_{11} and other atoms on edge #1. Similarly, C_1 and C_3 are used to obtain E_{21} and other atoms on edge #2. Then, the atoms in the row just below edge #0 are computed from E_{11} and E_{21} and so on. The entire process is depicted in Fig. 2.

Mapping of edges: Edges on composite surfaces are always shared by more than one facet. Since at first the facets are defined individually, two different instances exist for atoms on edges. It has to be ensured that for every atom only one instance remains in the representation. This can be achieved by introducing a *mapping* array that contains information about all neighboring faces and the edges they share. A typical row in this array looks like {a, b, ‘r’, c, d, ‘h’}. This basically implies that edge #b of face #a which is rectangular (‘r’) is the same as the edge #d of face #c

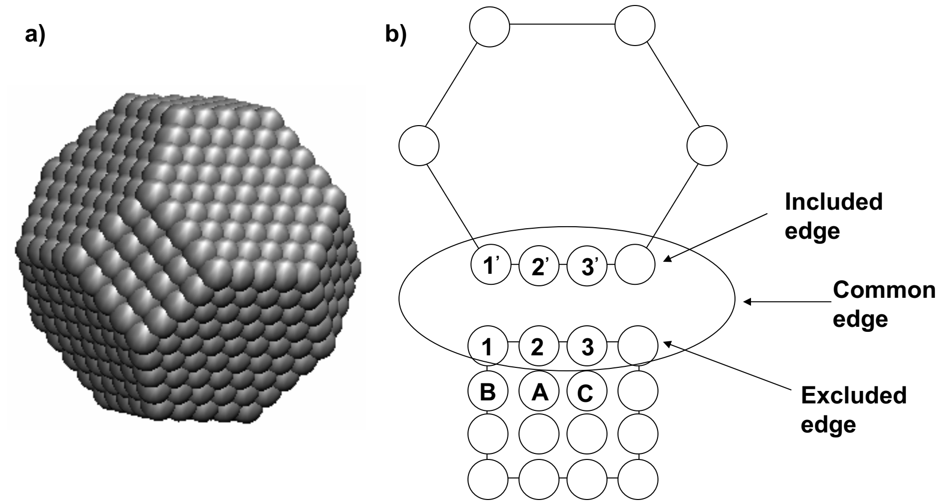

Figure 1: (a) Model surface of a cubo-octahedral nanoparticle (b) The unification process. The two facets illustrated have an edge in common. When the connected representation is first obtained for individual faces, the atom A stores, among others, atom 2 as one of its neighbors. But during the unification the atoms marked 1, 2, 3, etc. that lie on the 'excluded' edge are dropped. Instead, the atoms from the 'included' edge marked 1', 2', 3', etc. are retained. Thus, the atom A now points to atom 2' instead of 2 as one of its neighbors and vice versa. The unification process ends once this step is completed for all rows in the mapping array.

which is hexagonal ('h'). For every such row the edge that appears first is termed as the 'included' edge and the one that appears next as the 'excluded' edge.

The unification: In this step the *mapping* array is traversed one row at a time. By convention, the edge atoms on the 'excluded' edge are the ones that will be left out. But before that can be done, the neighbors of this 'excluded' edge have to be linked to the corresponding atoms on the 'included' edge and vice-versa. This is illustrated in Fig. 1b. Once the neighborhood-network is set up, all the included atoms are scanned and placed in a single 1-D array, thereby completing the connected representation of the cubo-octahedral nanoparticle.

ORR ON Pt NANOPARTICLES IN ACIDIC ELECTROLYTE

There have been a number of fundamental experimental and computational studies on the ORR at low index Pt surfaces ((111), (110), and (100)), both in acidic and basic electrolyte [2, 3, 7, 24, 25, 26], as well as at the Pt/Nafion interface [27, 28, 29]. Based on these studies, in this section we present a brief discussion of the elementary reaction steps in the ORR on Pt-based catalysts with emphasis on their kinetic aspect. The purpose is to compile a plausible reaction mechanism which is used for the detailed kinetic simulations using DMC presented below.

A change in the apparent Tafel slope is usually attributed to a change in the rate determining step (rds). For the Pt/Nafion interface, two distinct Tafel slopes

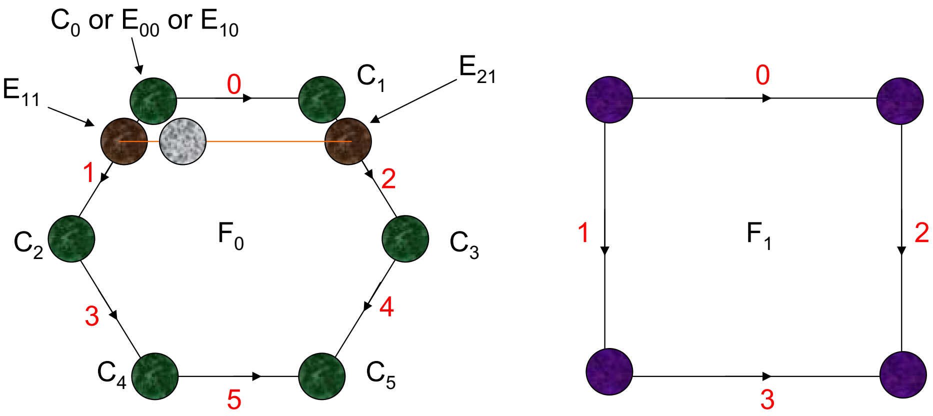

Figure 2: The numbering system used for generating connected representations. Besides an associated number, every edge also has a direction which is needed during the $unification$ step. All numbering in this method begins with the index 0. C_i denotes the corner atoms and the face numbers are denoted by F_i. All the corner atoms are provided as input for each face. E_{ij} symbolizes the jth atom of the ith edge.

are observed: approximately -60 mV/dec in the low current density (lcd) region, and approximately -120 mV/dec in the high current density (hcd) region. Thus, in the hcd region, the rds can be unambiguously identified with a single electron transfer step [24, 27, 28]. The situation is not straightforward in the lcd region. While some studies ascribe the low Tafel slope in the lcd region to a combination of chemical and electrochemical steps, namely oxygen adsorption and its subsequent first reduction step [27, 30], others assert that the rds is a single electron transfer step throughout [31, 3, 4]. Sepa *et al.* [31] have shown that by assuming Temkin adsorption, where the Gibbs free energy of activation for the rds increases linearly with surface coverage, the different Tafel slopes can still be explained within the premise that the rds is the same throughout. Careful experiments by Markovic *et al.* [32] also strongly suggest that adsorption of reaction intermediates on Pt(111) at high coverages by OH obey the Temkin adsorption isotherm. A similar conclusion was reached by Wang *et al.* [3] in a recent study, where it was shown that the deviation of the apparent Tafel slope from its intrinsic value (≈ -120 mV/dec) can be explained by mixed effects of site blocking and electronic effects (alteration in Gibbs free energy of adsorbed intermediates) of adsorbed OH without having to invoke a chemical step as rds in the lcd region. Furthermore, based on similarities in the apparent Tafel slope and voltammetry curves they concluded that the ORR reaction mechanism on Pt nanoparticle surfaces is the same as that on Pt(111), although the exchange current density was found to be an order of magnitude higher in the nanoparticle case. This was mainly ascribed to the increase in effective surface area [3]. Finally, for Pt(111) in acidic media with no specific adsorption of anions, ORR proceeds mostly via the four electron pathway between approximately 0.95 and 0.3 V [33]. Since Nafion electrolyte is indeed non-adsorbing [4], it follows from the discussion above that the following mechanism for ORR at the Pt/Nafion interface is a reasonable choice for the DMC simulations described below:

$$
\begin{aligned}
\mathrm{Pt_2 + O_2} &\underset{k_{-1}}{\overset{k_1}{\rightleftharpoons}} \mathrm{Pt_2.O_2} \\
\mathrm{Pt_2.O_2 + H^+}(aq) &\underset{k_{-2}}{\overset{k_2}{\rightleftharpoons}} \mathrm{Pt_2.O_2H} \\
\mathrm{Pt_2.O_2H} &\underset{k_{-3}}{\overset{k_3}{\rightleftharpoons}} \mathrm{Pt.O + Pt.OH} \\
\mathrm{Pt.O + H^+}(aq) &\underset{k_{-4}}{\overset{k_4}{\rightleftharpoons}} \mathrm{Pt.OH} \\
\mathrm{Pt.OH + H^+}(aq) &\underset{k_{-5}}{\overset{k_5}{\rightleftharpoons}} \mathrm{Pt.OH_2} \\
\mathrm{Pt.OH + Pt.OH} &\underset{k_{-6}}{\overset{k_6}{\rightleftharpoons}} \mathrm{Pt.O + Pt.OH_2} \\
\mathrm{Pt.OH_2} &\underset{k_{-7}}{\overset{k_7}{\rightleftharpoons}} \mathrm{Pt + H_2O}.
\end{aligned}
$$

This mechanism is also supported by first principles energy maps for the reaction intermediates [2, 25, 26]. Some aspects of this reaction mechanism will be discussed in the following.

Oxygen Adsorption

In ultra high vacuum (UHV) conditions, it is well established that on Pt(111), molecular oxygen adsorption dominates below 120 K, while the atomic oxygen adsorption process, for which the molecular adsorbed state is a precursor, is predominant between 170 and about 700 K [34, 35]. The scenario at the electrochemical interface may be different. Dissolved oxygen molecules will be in thermal equilibrium with the solution. At around 300 K this means less than approximately 0.1 eV translational energy for the oxygen molecules. These molecules, owing to their low energy, are most likely trapped in the physically adsorbed molecular state. Since dissociation to an atomically adsorbed state has high barrier heights [2, 36], it is likely that this step has to compete with other possible steps at the electrochemical interface, particularly the addition of a proton. Indeed, from the extensive kinetic analysis of their experimental data, Damjanovic *et al.* [24] proposed that if the molecular oxygen adsorption/desorption (reaction 1) is a fast quasi-equilibrium step, then the most likely next step is reaction 2, and that the proton is also involved in this rds in order to explain the pH dependence of the cathode reaction rate. Experiments of Markovic *et al.* [32, 37] on Pt catalysts in acidic media also suggest that there is no O-O bond breakage before reduction to a peroxide species. The barrier for Pt.OOH formation in the DFT studies by Sidik and Anderson [2] in the potential range of 0.5–1.2 V is about 0.5–0.6 eV, which is lower than the calculated 0.74 eV barrier for O_2 dissociation suggesting that O_2 does not dissociate before the first electron transfer step.

Surface OH and Water Adsorption/Desorption

Under operating conditions of PEMFC, the catalyst surface is covered with water, and so the reaction intermediates are solvated. At potentials larger than about 0.6

V, the observed oxidation current in cyclic voltammograms has been interpreted as the oxidation of H_2O to OH_{ads}, and accordingly, the "butterfly regions" of these voltammograms are explained as the reversible formation of OH_{ads} [38]. Wroblowa *et al.* [39] obtained the same potential versus coverage dependence of O-containing species with or without the presence of dissolved oxygen in the electrolyte solution. This clearly indicates that there is water consumption by the reverse of reaction 5 at the electrode. Ab initio MP2 calculations of Anderson *et al.* [40] also show that adsorbed H_2O can deprotonate with low activation energies at or above about 0.57 V to form OH_{ads}. This phenomenon is related to the potential of zero charge (pzc) of Pt(111) in dilute acids. By comparing different studies, Anderson *et al.* [40] have argued that the pzc in this case is about 0.6 V. At the pzc, there is direct involvement of the lone electron pair of the water O-atom in the adsorption of water at the electrochemical interface, similar to the metal/gas interface. It is noteworthy that above the pzc the water dipole is mostly in antiparallel orientation with respect to the electric field [41]. Thus, as the potential becomes more positive than the pzc, water is expected to bond more strongly to the surface [42, 43].

Calculation of Rate Constants

The expressions used for calculating the rate constants depend on the nature of the specific reactions. Rate coefficients for adsorption events are given by

$$k_{\text{ads}} = \frac{cS_0}{\Gamma}\sqrt{\frac{RT}{2\pi M}}, \tag{5}$$

where c is the concentration ($1/\text{m}^3$) of the molecule, S_0 is the sticking coefficient, Γ is the density of catalyst sites (1.52×10^{19} m^{-2} for Pt(111)), R is the universal gas constant (J/mol/K), and M is the mass of a single molecule (kg). A value of 0.3 was taken for S_0 corresponding to molecularly adsorbed oxygen [44]. It should be pointed out here that the calculation of transition probabilities inherently considers the fact that two adjacent sites are needed for bimolecular adsorption of oxygen. Hence, in Eq. 5, Γ has an exponent of unity both for uni- and bi-molecular adsorption. For the reduction reactions, the rate coefficients are computed as

$$k_{\text{EC}} = \kappa k_0 \exp(\frac{-E_{\text{act}}}{k_B T}), \tag{6}$$

where κ, the electronic transmission coefficient, was taken as unity in this work. k_0 includes the details of the proton transfer and has a value of approximately 200 s^{-1} sites^{-1} [25]. Rate coefficients for the oxidation steps were obtained so that the reduction/oxidation steps are thermodynamically consistent at the corresponding standard potential. The activation energies, E_{act}, for electrochemical reactions vary with the electrode potential and were taken from the work of Anderson *et al.* [2]. Finally, the rate coefficients for the reaction steps 3 and 6 are given as

$$k_{\text{chem}} = \frac{k_B T}{h}\frac{f_{\text{act}}}{f_{\text{react}}}\exp(\frac{-E_{\text{act}}}{k_B T}), \tag{7}$$

where f_{act} and f_{react} are the partition functions with respect to the zero-point level of the molecule for saddle point and reactants respectively (with the imaginary frequency

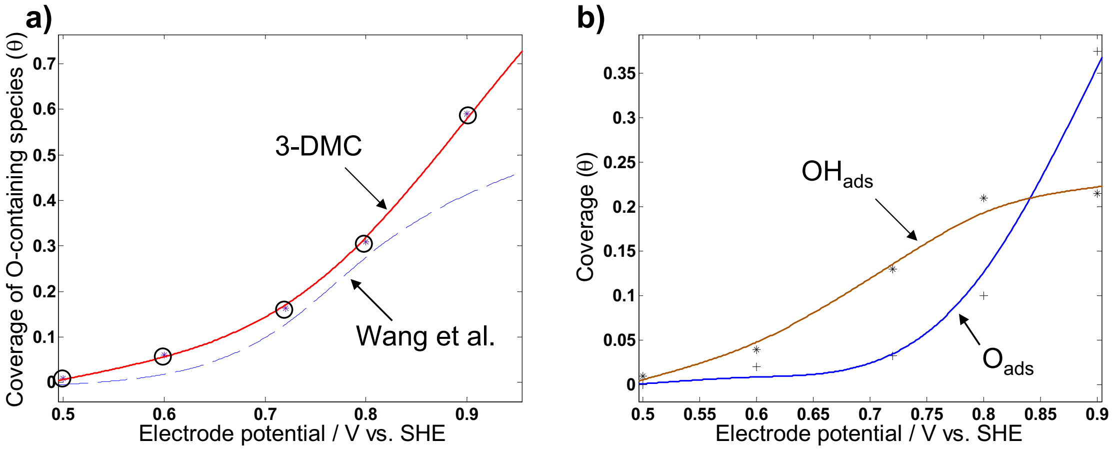

Figure 3: (a) Total coverage of O-containing species (b) coverage of adsorbed O and OH obtained from DMC simulations. The solid lines are smooth fits to the data points obtained from DMC simulations.

excluded in the case of the saddle point) and E_{act} is the activation energy including a zero-point correction. Our calculations indicate that the forward reaction 3 is very fast. Reaction 6 was also found to be fast in either direction. For the desorption of water (reverse of reaction 7) the normal prefactor $\approx 10^{13}$ s^{-1} was assumed. The activation energy, E_{act}, was taken as 53 kJ/mol [45]. The water adsorption rate coefficient can then be calculated from the equilibrium constant $K_{\mathrm{w}} = k_{-7}/k_7 = \exp(-\Delta G/k_B T)$, where ΔG is the Gibbs free energy change for the adsorption of water (reverse of reaction 7) and was estimated from the data in refs [25], [46]. A more complete discussion of the rate coefficients for the reaction mechanism presented above is in preparation and will be reported elsewhere.

RESULTS AND DISCUSSIONS

The ORR mechanism presented above was simulated on a Pt nanoparticle of approximately 10 nm in diameter. The nanoparticle was assumed to have cubo-octahedral surface. Rate data for Pt(100) sites was taken the same as that for Pt(111) as complete data for Pt(100) is not available at present. Hence, the results presented here are essentially for Pt(111) and will be compared to experimental results for Pt(111). Interactions between the adsorbed intermediates, referred to as *electronic effects*, were not considered. Total coverages (θ) of O-containing species ($\mathrm{O_{ads}}$ and $\mathrm{OH_{ads}}$) at steady state are shown is Fig. 3a as a function of the electrode potential with respect to standard hydrogen electrode. As can be seen, these values compare well with a recent experimental study of Wang *et al.* [3], except at high potentials near 0.9 V. This discrepancy might be explained by the fact that electronic effects were not included in this work. It is clear that as the potential increases, there is increased coverage by O-containing species which act as site-blocking species, thereby inhibiting oxygen reduction. It is worth mentioning that in the simulations nearly all the adsorbed O-containing species were found to come from the dissociation of water, which is consistent with the existing interpretation [39, 47]. Figure 3b shows the surface coverage of $\mathrm{O_{ads}}$ and $\mathrm{OH_{ads}}$. Although θ_{OH} is higher than θ_{O} below $\sim$0.8

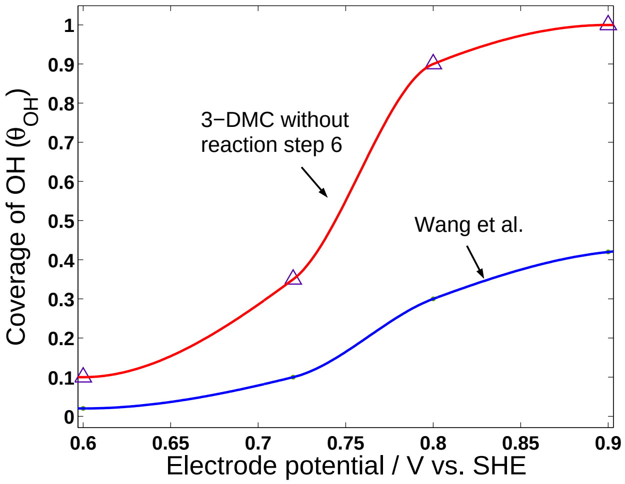

Figure 4: Surface coverage of adsorbed OH from simulations of the ORR mechanism given in text without the LH reaction (step 6). The experimental data of Wang *et al.* [3] may have some contribution from adsorbed O. Hence, experimentally determined OH coverage will be lower than as shown in this figure.

V, coverage of atomic oxygen is found to increase rapidly around 0.85 V. A similar conclusion was reached by Wroblowa *et al.* [39] by comparing saturation coverages at various metal electrodes including Pt. However, accounting for interactions due to the presence of OH_{ads} is likely to reduce the coverage of O_{ads}. Finally, we study the sensitivity of the results for reaction step 6. Simulation results of a mechanism without reaction 6, but everything else remaining the same, are shown in Fig. 4. It is apparent that this Langmuir-Hinshelwood (LH) type reaction seems to have a marked effect on the steady state coverages. It will be interesting to investigate the role of this step in the presence of electronic effects, which is the subject of an ongoing study.

CONCLUSIONS

A new approach, 3-DMC, for DMC simulations of surface chemistry on real catalyst nanoparticle surfaces was introduced. Steady state coverages of O-containing species obtained from simulations of a detailed reaction mechanism for ORR on Pt nanoparticles in acidic media, using this approach were compared with experimentally observed surface coverages, showing good agreement. Substantial presence of O_{ads} around 0.9 V is predicted. The simulations also suggest that an LH type reaction (step 6) is very important. Further studies are underway to better understand the influence of including electronic effects on the coverage of O_{ads} at high potentials ($\sim$0.9 V) and the role of reaction 6.

ACKNOWLEDGEMENTS

This work is supported by Honda R&D CO.,Ltd., Wako, Japan. The authors also thank Prof. A. B. Anderson for fruitful discussions on the ORR mechanism.

References

1. L. Carrette, K. A. Friedrich and U. Stimming, *Fuel Cells*, **1**(1), 5 (2001).
2. R. A. Sidik and A. B. Anderson, *J. Electroanal. Chem.*, **528**, 69 (2002).
3. J. X. Wang, N. M. Markovic and R. R. Adzic, *J. Phys. Chem. B.*, **108**, 4127 (2004).
4. N. M. Markovic, T. J. Schmidt, V. Stamenkovic and P. N. Ross, *Fuel Cells*, **1**(2), 105 (2001).
5. K. Kinoshita, *Electrochemical Oxygen Technology*, John Wiley & Sons (1992).
6. J. Wintterlin, R. Schuster and G. Ertl, *Phys. Rev. Lett.*, **77**(1), 123 (1996).
7. N. M. Markovic, H. A. Gasteiger, B. N. Grgur and P. N. Ross, *J. Electroanal. Chem.*, **467**, 157 (1999).
8. R. Danielak, A. Perera, M. Moreau, M. Frankowicz and R. Karpal, *Physica A*, **229**, 428 (1996).
9. R. Kissel-Osterrieder, F. Behrendt and J. Warnatz, *Proc. Comb. Inst.*, **28**, 1323 (2000).
10. R. Kissel-Osterrieder, F. Behrendt and J. Warnatz, *Proc. Comb. Inst.*, **27**, 2267 (1998).
11. V. P. Zhdanov, *Phys. Rev. E*, **67**, 042601 (2003).
12. J. J. Lukkien, J. P. L. Segers, P. A. J. Hilbers, R. J. Gelten and A. P. J. Jansen, *Phys. Rev. E*, **58**(2), 2598 (1998).
13. D. S. Mainardi, S. R. Calvo, A. P. J. Jansen, J. J. Lukkien and P. B. Balbuena, *Chem. Phys. Lett.*, **382**, 553 (2003).
14. J. S. Reese, S. Raimondeau and D. G. Vlachos, *J. Comput. Phys.*, **173**, 302 (2001).
15. A. B. Bortz, M. H. Kalos and J. L. Lebowitz, *J. Comput. Phys.*, **17**, 10 (1975).
16. G. Korniss, M. A. Novotny and P. A. Rikvold, *J. Comp. Phys.*, **153**, 488 (1999).
17. P. Araya, W. Porod, R. Sant and E. E. Wolf, *Surf. Sc. Lett.*, **208**, L80 (1988).
18. A. S. McLeod and L. F. Gladden, *J. of Catal.*, **173**, 43 (1998).
19. K. Binder and D. W. Heermann, *Monte Carlo Simulation in Statistical Physics*, Springer (1992).
20. G. Brown, P. A. Rikvold, S. J. Mitchell and M. A. Novotny, in A. Wieckowski, (Editor) *Interfacial Electrochemistry: Theory, Experiment, and Applications*, 47–61, Marcel Dekker, New York (1999).
21. V. Zhdanov and B. Kasemo, *Surf. Sc. Rep.*, **39**, 25 (2000).

22. D. G. Vlachos, L. D. Schmidt and R. Aris, *Surf. Sc.*, **249**, 248 (1991).

23. A. P. J. Jansen, *Comp. Phys. Comm.*, **86**, 1 (1995).

24. A. Damjanovic and V. Brusic, *Electrochimica Acta*, **12**, 615 (1967).

25. J. K. Norskov, J. Rossmeisl, A. Logadottir, L. Lindqvist, J. R. Kitchin, T. Bligaard and H. Jonsson, *J. Phys. Chem. B*, **108**, 17886 (2004).

26. A. Panchenko, M. T. M. Koper, T. E. Shubina and S. J. Mitchell, *J. Electrochem. Soc.*, **151**(12), A2016 (2004).

27. A. Parthasarathy, C. R. Martin and S. Srinivasan, *J. Electrochem. Soc.*, **138**, 916 (1991).

28. L. Zhang, C. Ma and S. Mukherjee, *J. Electroanal. Chem.*, **568**, 273 (2004).

29. F. A. Uribe, T. E. Springer and S. Gottesfeld, *J. Electrochem. Soc.*, **139**(3), 765 (1992).

30. E. Yeager, *Electrochimica Acta*, **29**, 1527 (1984).

31. D. B. Sepa, M. V. Vojnovic and L. M. Vracer, *Electrochimica Acta*, **29**, 1169 (1984).

32. N. M. Markovic, H. A. Gasteiger, B. N. Grgur and P. N. Ross, *J. Electroanal. Chem.*, **467**, 157 (1999).

33. T. J. Schmidt, U. A. Paulus, H. A. Gasteiger and R. J. Behm, *J. Electroanal. Chem.*, **508**, 41 (2001).

34. G. Fisher and Gland, *Surf. Sci.*, **95**, 587 (1980).

35. P. D. Nolan, B. R. Lutz, P. L. Tanaka, J. E. Davis and C. B. Mullins, *J. Chem. Phys.*, **111**(8), 3696 (1999).

36. A. Eichler and J. Hafner, *Phys. Rev. Lett.*, **79**, 4481 (1997).

37. V. Stamenkovic, N. M. Markovic and P. N. Ross Jr., *J. Electroanal. Chem.*, **500**, 44 (2000).

38. N. M. Markovic, T. J. Schmidt, B. N. Grgur, H. A. Gasteiger, R. J. Behm and P. N. Ross, *J. Phys. Chem. B*, **103**, 8568 (1999).

39. H. S. Wroblowa, M. L. B. Rao, A. Damjanovic and J. O. Bockris, *J. Electroanal. Chem.*, **1**, 139 (1967).

40. A. Anderson, N. Neshev, R. Sidik and P. Shiller, *Electrochimica Acta*, **47**(18), 2999 (2002).

41. T. Iwasita and X. Xia, *J. Electroanal. Chem.*, **411**, 95 (1996).

42. I.-C. Yeh and M. L. Berkowitz, *J. Electroanal. Chem.*, **450**, 313 (1998).

43. J. W. Halley, A. Mazzolo, Y. Zhou and D. Price, *J. Electroanal. Chem.*, **450**, 273 (1998).

44. A. C. Luntz, M. D. Williams and D. S. Bethune, *J. Phys. Chem.*, **89**(7), 4381 (2000).

45. J. L. Daschbach, B. M. Peden, R. S. Smith and B. D. Kay, *J. Chem. Phys.*, **120**(3), 1516 (2004).

46. A. Michaelides and P. Hu, *J. Am. Chem. Soc.*, **123**, 4235 (2001).

47. R. R. Adzic, in D. D. Scherson, D. Tryk and X. Xing, (Editors) *Structural Effects in Electrocatalysis and Oxygen Electrochemistry*, volume 92, 419, The Electrochemical Soc. Inc.: Pennington (1992).